

## Critical Metallicity of Cool Supergiant Formation. II. Physical Origin

PO-SHENG OU (歐柏昇)<sup>1,2</sup> AND KE-JUNG CHEN (陳科榮)<sup>1,3</sup>

<sup>1</sup>*Institute of Astronomy and Astrophysics, Academia Sinica, No.1, Sec. 4, Roosevelt Rd., Taipei 10617, Taiwan, R.O.C.*

<sup>2</sup>*Department of Physics, National Taiwan University, No.1, Sec. 4, Roosevelt Rd., Taipei 10617, Taiwan, R.O.C.*

<sup>3</sup>*Heidelberg Institute for Theoretical Studies, Schloss-Wolfsbrunnenweg 35, Heidelberg 69118, Germany*

### ABSTRACT

This study investigates the physical origin of the critical metallicity ( $Z_c \sim 0.001$ ) required for the formation of cool supergiants, as revealed by stellar evolution models. Using model grids that vary in mass, metallicity, opacity, and nuclear reaction rates, we identify a threshold terminal-age main-sequence (TAMS) radius ( $R_T$ ) that determines whether a star of a given mass can evolve into the red supergiant (RSG) phase. Through stellar models and homology relations, we show that metallicity affects the TAMS radius via its influence on opacity and nuclear energy generation. By classifying the evolutionary pathways of supergiants, we demonstrate how TAMS radius, shaped by metallicity, decisively governs the post-main-sequence outcome: Stars with metallicities  $Z < Z_c$  exhibit TAMS radii smaller than  $R_T$  and proceed to advanced core helium or carbon burning while retaining compact envelopes, thereby preventing further expansion into the RSG regime. In contrast, stars with  $Z > Z_c$  have TAMS radii larger than  $R_T$  and expand into the stable RSG phase during core helium burning. The envelope radius at the onset of core helium burning is the key factor determining whether a star becomes a red or blue supergiant. Our results explain the origin of the critical metallicity and offer insight into the evolution of metal-poor massive stars in the early universe.

*Keywords:* Supergiant Stars — Red Supergiant Stars — Stellar Evolution — Metallicity

### 1. INTRODUCTION

In the first paper of this series (Ou et al. 2023, hereafter Paper I), we presented a grid of  $\sim 2000$  stellar models and identified a critical metallicity for the formation of cool supergiants (i.e., red or yellow),  $Z_c \sim 0.001 \approx 0.1Z_\odot$  (For reference,  $Z_\odot = 0.0134$ ; Asplund et al. 2009). We found that massive stars with metallicities below this threshold ( $Z < Z_c$ ) typically do not evolve into cool supergiants during the core-helium (He) burning phase. This bifurcation in evolutionary paths has a significant impact on stellar mass loss, as cool supergiants exhibit considerably higher mass-loss rates than main-sequence stars. In this paper, we further explore the physical origin of this critical metallicity.

Our finding of a critical metallicity is consistent with various earlier stellar models, which likewise show that low- $Z$  stars tend to remain blue supergiants (BSGs) rather than evolving into red supergiants (RSGs) (Brunish & Truran 1982; Arnett 1991; Baraffe & El Eid 1991; Brocato & Castellani 1993; Hirschi 2007; El Eid et al. 2009; Limongi 2017). Similarly, in the Hertzsprung–Russell (HR) diagram of the recent Geneva stellar evolution models, stars with  $Z = 0.0004$  also remain blue during the core-He burning phase (Groh et al. 2019). These results suggest that the existence of a critical metallicity is a general outcome among various stellar evolution models.

Although the metallicity dependence of RSG formation is consistent between models, the underlying physics behind the effect of metallicity remains uncertain. An early attempt to explain it was made by Ritossa (1996), who argued that the envelopes of low-metallicity stars cannot effectively trap radiation energy from central burning because of reduced opacity. Therefore, they cannot evolve into RSGs. This interpretation is based on a framework in which thermal imbalance within the envelope, governed by the core luminosity and the envelope opacity, drives the inflation of the stellar envelope towards red-giant or supergiant dimensions (Renzini 1984; Renzini et al. 1992; Renzini & Ritossa 1994; Renzini 2023). However, this explanation for RSG formation based

on heat absorption has been questioned by subsequent studies (Iben 1993; Sugimoto & Fujimoto 2000; Faulkner 2005; Miller Bertolami 2022).

Understanding the metallicity effect on RSG formation is closely tied to the long-standing question: Why do stars become red supergiants? In our recent study (Ou & Chen 2024), we revisited this question and identified the physical criteria that determine whether a star can evolve into the RSG phase. Building on those results, we now aim to investigate how metallicity influences RSG<sup>1</sup> formation to identify the physical origin of the critical metallicity using stellar models.

In Section 2, we briefly describe the models employed in this study. In Section 3, we present a series of numerical experiments to investigate the metallicity effect on supergiant evolution. Section 4 identifies a threshold radius at the end of main sequence for RSG formation and explores its dependence on mass. To explore the connection between metallicity and this threshold radius, Section 5 studies how metallicity influences stellar radii. Section 6 classifies the evolutionary pathways for stellar models with different masses and metallicities, using the RSG formation criteria proposed by Ou & Chen (2024). In Section 7, we offer a physical interpretation of the threshold radius and critical metallicity based on the core properties. Finally, Section 8 discusses the broader implications of our findings and concludes the paper.

## 2. MODELS

We begin with the grid of massive star models from Paper I, which spans initial masses from 11 to  $60M_{\odot}$  and metallicities from  $Z = 1 \times 10^{-5}$  to  $2 \times 10^{-2}$ . The models were computed using the Modules for Experiments in Stellar Astrophysics (MESA; Paxton et al. 2011, 2013, 2015, 2018, 2019; Jermyn et al. 2023) version No. 10108. Each model evolves from the pre-main-sequence stage using the “basic” nuclear reaction network with eight isotopes, and then proceeds from the zero-age main sequence (ZAMS) using the “approx21 (Cr60)” network, which includes 21 isotopes. The models incorporate Henyey’s mixing-length theory, semi-convection, convective overshooting, Type 2 opacity, and mass loss. Details of the model setup are provided in Section 2 of Paper I.

Following the analysis in Paper I, we adopt the  $25M_{\odot}$  models as representative cases, as they exhibit typical evolutionary behaviors across different metallicities. Using these  $25M_{\odot}$  models from the grid described above, we carry out a series of experiments on stellar models by modifying the opacity and nuclear reaction rates to examine their effects on supergiant evolution. These extended models are designed as numerical experiments to isolate the influence of specific physical parameters and are not intended to represent realistic stellar evolution.

Opacity, as a metallicity-dependent factor, strongly impacts the energy transport of the entire star. Adjusting opacity in stellar models requires careful consideration as opacity is coupled with the evolution of gas density, temperature, and metallicity. A robust method to modify opacity is by adjusting the value of  $Z_{\text{base}}$  in MESA, which specifies the base metallicity used to retrieve opacities from the opacity tables. Importantly,  $Z_{\text{base}}$  governs the opacity alone and does not represent the metallicity of the star. For example, a model with  $Z = 0.02$  and  $Z_{\text{base}} = 0.001$  has a metallicity of 0.02 but evolves with an opacity comparable to that of a star with  $Z = 0.001$ . This approach enables us to isolate the effects of opacity from other metallicity-dependent effects in stellar evolution. To avoid confusion in terminology, we denote the MESA input parameter  $Z_{\text{base}}$  as  $\zeta_{\text{opacity}}$  throughout the discussion in this paper.

Nuclear reaction rates are modified using the `reaction_for_special_factor` option in the `star_job` section of the MESA inlist. For the CNO cycle, we adopt the parameter  $\eta_{\text{CNO}}$  to linearly scale the rates of five key reactions included in the approx21 nuclear reaction network: (1)  $^{12}\text{C} + ^1\text{H} \rightarrow ^{13}\text{N} + \gamma$ , (2)  $^{14}\text{N} + ^1\text{H} \rightarrow ^{15}\text{O} + \gamma$ , (3)  $^{16}\text{O} + ^1\text{H} \rightarrow ^{17}\text{F} + \gamma$ , (4)  $^{15}\text{N} + ^1\text{H} \rightarrow ^{16}\text{O} + \gamma$ , and (5)  $^{15}\text{O} + ^1\text{H} \rightarrow ^{12}\text{C} + ^4\text{He}$ . In addition, we use another factor  $\eta_{3\alpha}$  to linearly scale the reaction rate of the triple-alpha process.

We also designed an experiment in which the CNO reaction rates are modified only during the shell H-burning phase in the post-main-sequence stage. Specifically, the adjustment is applied once the He core has formed and is limited to regions outside the core. By default in MESA, the He core is defined as the region where the H mass fraction satisfies  $X_{\text{H}} \leq 0.1$ . For this experiment, we used the factor  $\eta_{\text{shellCNO}}$  to linearly scale the CNO reaction rates in the H burning shell.

In addition to the extensive grid of stellar models with varying masses and metallicities presented in Paper I, we have constructed four new distinct grids of MESA models spanning different parameter spaces. In total, these five grids contain 6,896 models. A summary of the model configurations is provided below and in Table 1.

- (a) Initial stellar mass ( $M_i$ ) and metallicity ( $Z$ ), from Paper I.
- (b) Metallicity ( $Z$ ) and opacity (set by  $\zeta_{\text{opacity}}$ ).

<sup>1</sup> We briefly clarify our use of the terms “red supergiant” and “cool supergiant.” In Paper I, we adopted the term cool supergiant to describe massive stars that expand to  $\gtrsim 1,000R_{\odot}$ . We avoided the conventional term red supergiant because very massive stars (e.g.,  $\gtrsim 50M_{\odot}$ ) often maintain effective temperatures above 4,000K, placing them in the yellow rather than strictly defined red regime. Nevertheless, from a physical standpoint in terms of stellar radius, such stars do not differ intrinsically from classical red supergiants. Moreover, in this paper, our focus is mainly on stars with  $\lesssim 30M_{\odot}$ , which cool below 4,000K and fulfill the criteria of red supergiants. Therefore, we adopt the more common term red supergiant throughout this work.

- (c) Hydrogen-burning rate (scaled by  $\eta_{\text{CNO}}$ ) and opacity (set by  $\zeta_{\text{opacity}}$ ).
- (d) Shell Hydrogen-burning rate (scaled by  $\eta_{\text{shellCNO}}$  for the burning shell) and opacity (set by  $\zeta_{\text{opacity}}$ ).
- (e) Helium-burning rate (scaled by  $\eta_{3\alpha}$ ) and opacity (set by  $\zeta_{\text{opacity}}$ ).

Grid (a), as presented in Paper I, consists of realistic stellar models used to demonstrate the existence of a critical metallicity. On the other hand, the models in Grids (b)–(e) are not intended to represent realistic stars; instead, they act as experimental models to investigate the effects of specific stellar parameters. For comparison, we vary only two parameters in each grid of models, with all other parameters identical to those in Grid (a). Grids (b)–(e) are based on  $25 M_{\odot}$  stars, with Grids (c)–(e) further restricted to  $Z = 0.001$ .

**Table 1.** Summary of model grids and varied parameters

Grid	$M_i (M_{\odot})$	$Z$	$\zeta_{\text{opacity}}$	$\eta_{\text{CNO}}$	$\eta_{\text{shellCNO}}$	$\eta_{3\alpha}$
(a)	11, 12, 13, ..., 59, 60	$(1, 2, \dots, 9) \times 10^{-5}$ , $(1, 2, \dots, 9) \times 10^{-4}$ , $(1, 2, \dots, 9) \times 10^{-3}$ , $(1.0, 1.1, \dots, 2.0) \times 10^{-2}$	1.0	1.0	1.0	1.0
(b)	25	$(1, 2, \dots, 9) \times 10^{-5}$ , $(1, 2, \dots, 9) \times 10^{-4}$ , $(1, 2, \dots, 9) \times 10^{-3}$ , $(1.0, 1.1, \dots, 2.0) \times 10^{-2}$	$(1, 2, \dots, 9) \times 10^{-5}$ , $(1, 2, \dots, 9) \times 10^{-4}$ , $(1, 2, \dots, 9) \times 10^{-3}$ , $(1.0, 1.1, \dots, 2.0) \times 10^{-2}$	1.0	1.0	1.0
(c)	25	0.001	$(1, 2, \dots, 9) \times 10^{-5}$ , $(1, 2, \dots, 9) \times 10^{-4}$ , $(1, 2, \dots, 9) \times 10^{-3}$ , $(1, 2, 3, 4, 5) \times 10^{-2}$	$(1, 2, \dots, 9) \times 10^{-3}$ , $(1, 2, \dots, 9) \times 10^{-2}$ , $(1, 2, \dots, 9) \times 10^{-1}$ , $(1, 2, \dots, 10)$	1.0	1.0
(d)	25	0.001	$(1, 2, \dots, 9) \times 10^{-5}$ , $(1, 2, \dots, 9) \times 10^{-4}$ , $(1, 2, \dots, 9) \times 10^{-3}$ , $(1, 2, 3, 4, 5) \times 10^{-2}$	1.0	$(1, 2, \dots, 9) \times 10^{-3}$ , $(1, 2, \dots, 9) \times 10^{-2}$ , $(1, 2, \dots, 9) \times 10^{-1}$ , $(1, 2, \dots, 10)$	1.0
(e)	25	0.001	$(1, 2, \dots, 9) \times 10^{-5}$ , $(1, 2, \dots, 9) \times 10^{-4}$ , $(1, 2, \dots, 9) \times 10^{-3}$ , $(1, 2, 3, 4, 5) \times 10^{-2}$	1.0	1.0	$(1, 2, \dots, 9) \times 10^{-3}$ , $(1, 2, \dots, 9) \times 10^{-2}$ , $(1, 2, \dots, 9) \times 10^{-1}$ , $(1, 2, \dots, 10)$

**Notes.**

$M_i$ : Initial stellar mass.

$Z$ : Stellar metallicity.

$\zeta_{\text{opacity}}$ : Equivalent to the base metallicity ( $Z_{\text{base}}$ ) adopted for used for interpolating opacity in the tables, not to be confused with the star's metallicity  $Z$ .

$\eta_{\text{CNO}}$ : Scaling factor for the CNO cycle reaction rate.

$\eta_{\text{shellCNO}}$ : Scaling factor for the CNO cycle reaction rate, applied only to the H-burning shell.

$\eta_{3\alpha}$ : Scaling factor for the triple-alpha reaction rate.

### 3. NUMERICAL EXPERIMENTS ON OPACITY AND NUCLEAR REACTION RATES

Metallicity affects stellar evolution through its impact on several key physical quantities, including opacity, nuclear burning rates, and mean molecular weight (e.g., [El Eid et al. 2009](#)). In this section, to disentangle the primary factors through which

metallicity impacts evolution toward the supergiant phase, we conduct a series of experiments for  $25M_{\odot}$  stars using Grid (b)–(e), as described in Section 2. In particular, we focus on the roles of opacity and nuclear reaction rates.

For each model in these grids, we assess whether it evolves into an RSG by calculating the maximum radius it reaches during the core He-burning phase, prior to the onset of core carbon (C) burning. This maximum radius is denoted as  $R_{\max}$ .

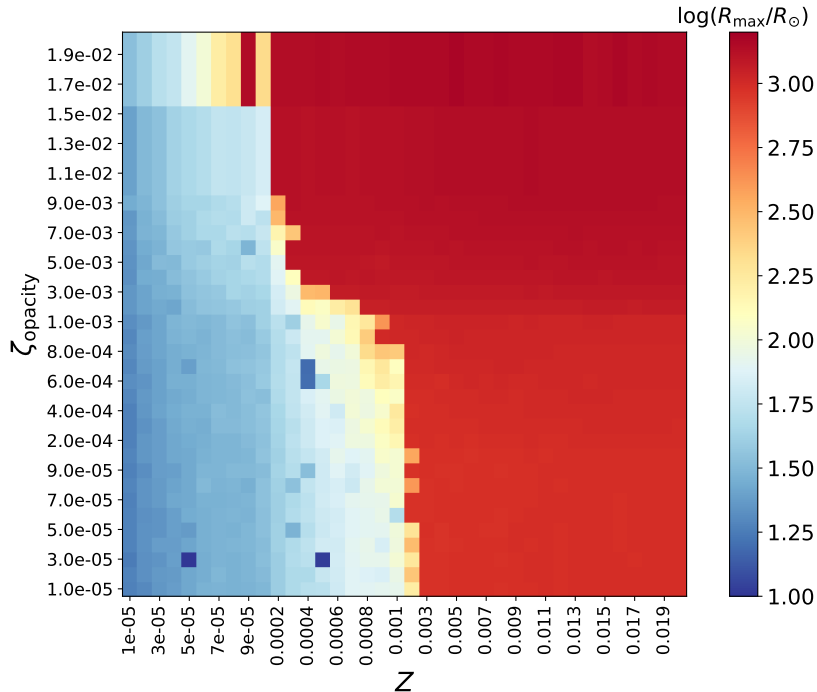


**Figure 1.** Maximum stellar radius during the core He-burning stage ( $R_{\max}$ ) for Grid (b), which includes models with an initial mass of  $25M_{\odot}$ , varying in metallicity ( $Z$ ) and opacity parameter ( $\zeta_{\text{opacity}}$ ). The boundary between red and blue supergiants depends on  $\zeta_{\text{opacity}}$  in the metallicity range  $Z \gtrsim 10^{-3}$ , but becomes nearly insensitive to  $\zeta_{\text{opacity}}$  when  $Z \lesssim 10^{-3}$ .

### 3.1. Grid (b): Metallicity and Opacity

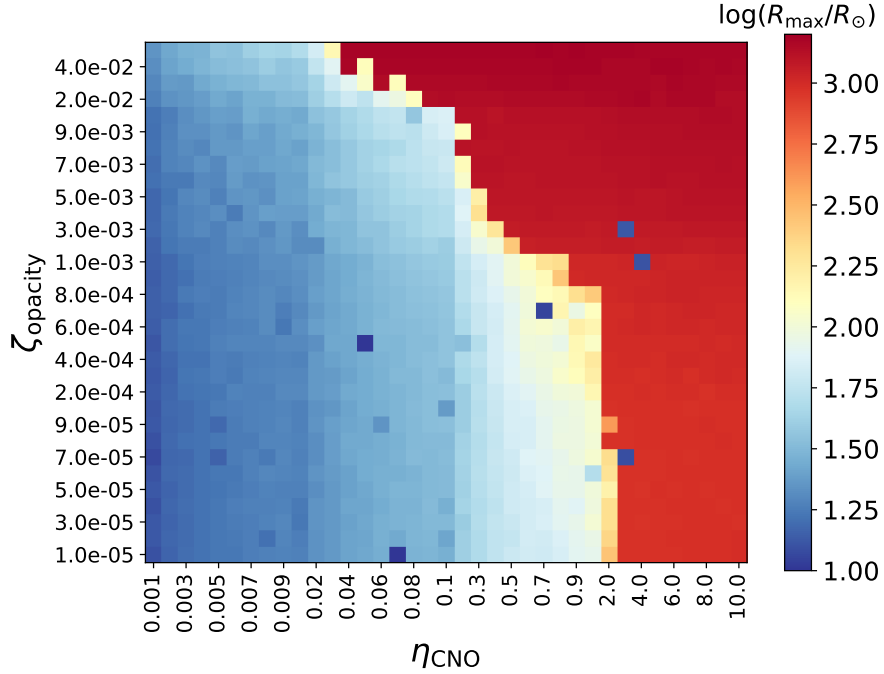
We begin by examining the effect of opacity on envelope expansion by constructing a grid of stellar models, Grid (b), with varying metallicities and opacities.

Figure 1 shows  $R_{\max}$  for each model in Grid (b). The models that reach RSG dimensions ( $\log(R/R_{\odot}) \gtrsim 3$ ) are clearly separated from those that remain within BSG dimensions ( $\log(R/R_{\odot}) \lesssim 2$ ). For  $Z \lesssim 10^{-3}$ , the boundary dividing these two areas is vertical, indicating that opacity, controlled by  $\zeta_{\text{opacity}}$ , has little influence on the supergiant outcome in this low- $Z$  range. Only when  $Z \gtrsim 10^{-3}$  does opacity begin to significantly affect whether the star becomes an RSG or remains a BSG. Notably, even with extremely low  $\zeta_{\text{opacity}}$  (a few times  $10^{-5}$ ), stars with  $Z \gtrsim 0.003$  can still expand to RSG dimensions. This suggests that additional metallicity-dependent factors, beyond opacity alone, play a role in determining the supergiant’s fate.

### 3.2. Grid (c): Hydrogen Burning Rates and Opacity

In addition to opacity, metallicity also significantly influences nuclear burning within a star. In our second experiment, Grid (c), we examine the combined effects of these two factors by varying both the opacity parameter  $\zeta_{\text{opacity}}$  and the linear scaling factor for the reaction rates of the CNO cycle,  $\eta_{\text{CNO}}$ . In this experiment,  $\eta_{\text{CNO}}$  is applied consistently throughout the entire stellar lifetime, scaling the reaction rates of both core H burning during the main-sequence phase and shell H burning during the post-main-sequence evolution.

Figure 2 shows  $R_{\max}$  for each model in Grid (c). A clear boundary separates models that evolve into RSGs from those that remain as BSGs. In general, both higher opacity and higher CNO reaction rates favor the transition to RSGs. When the opacity is low, a larger CNO rate is required for the star to expand to RSG radii. *In particular, even models with low opacity with  $\zeta_{\text{opacity}}$  on the order of a few times  $10^{-5}$  can still evolve into RSGs if CNO burning is sufficiently efficient (i.e.,  $\eta_{\text{CNO}} \geq 3$ ).*



**Figure 2.** Maximum stellar radius during the core He-burning stage ( $R_{\max}$ ) for Grid (c): models with an initial mass of  $25M_{\odot}$  and metallicity  $Z = 0.001$ , computed for varying values of the CNO-cycle reaction rate (scaled by  $\eta_{\text{CNO}}$ ) and opacity parameter ( $\zeta_{\text{opacity}}$ ). Both  $\eta_{\text{CNO}}$  and  $\zeta_{\text{opacity}}$  influence the evolutionary outcome, determining whether the star becomes a red or blue supergiant.

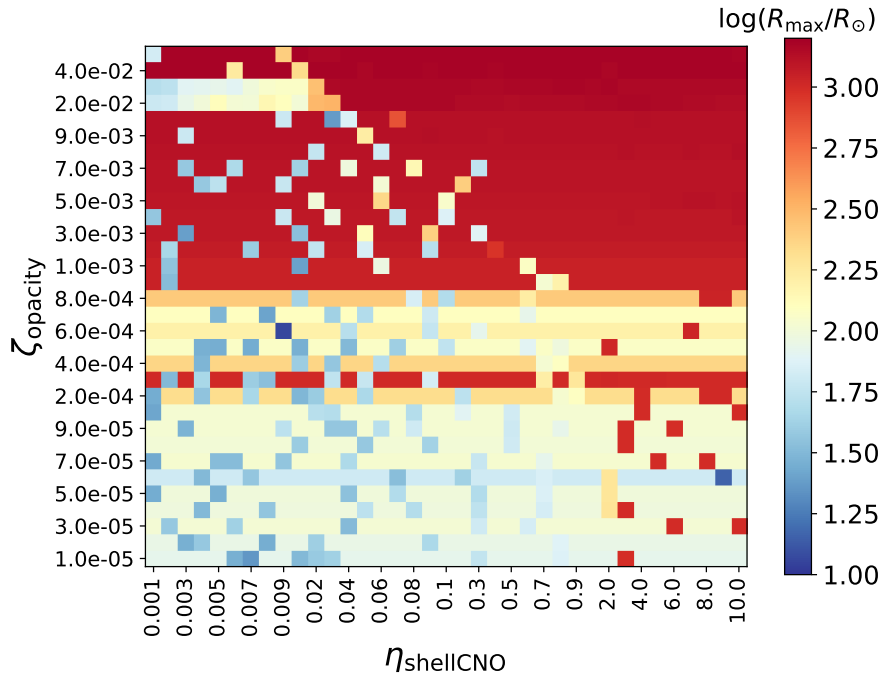


**Figure 3.** Maximum stellar radius during the core He-burning stage ( $R_{\max}$ ) for Grid (d): models with an initial mass of  $25M_{\odot}$  and metallicity  $Z = 0.001$ , computed for varying values of the CNO-cycle reaction rate during the shell H-burning stage (scaled by  $\eta_{\text{shellCNO}}$ ) and opacity parameter ( $\zeta_{\text{opacity}}$ ). For comparison, the parameter  $\eta_{\text{CNO}}$  used in Figure 2 is applied throughout all evolutionary stages, whereas  $\eta_{\text{shellCNO}}$  in this figure is applied only during the shell H-burning stage. While  $R_{\max}$  exhibits some scatter, the overall trend indicates that  $\eta_{\text{shellCNO}}$  has little impact on the supergiant outcome.

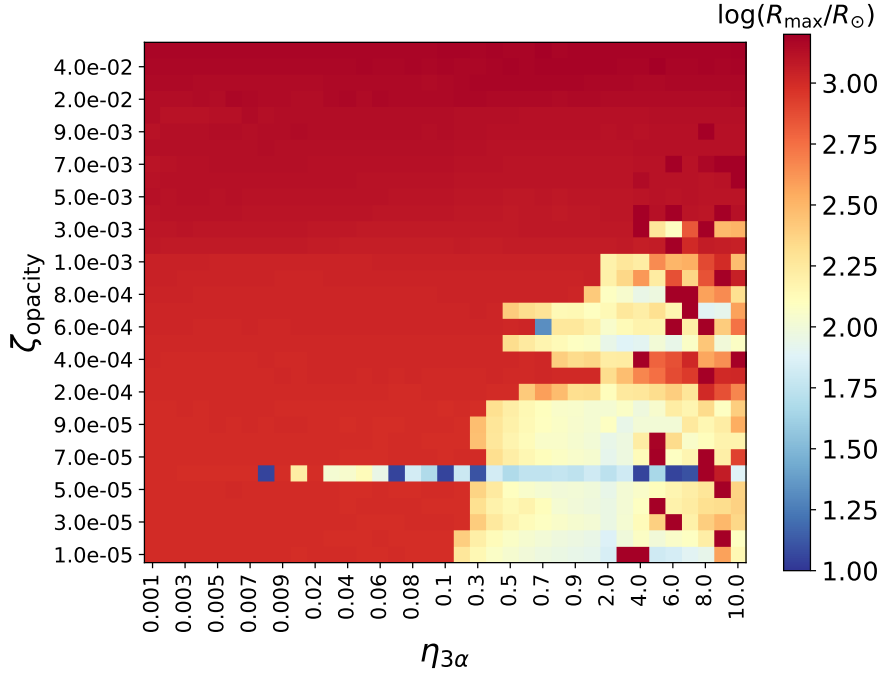


**Figure 4.** Maximum stellar radius during the core He-burning stage ( $R_{\max}$ ) for Grid (e): models with an initial mass of  $25M_{\odot}$  and metallicity  $Z = 0.001$ , computed for varying values of the triple-alpha reaction rate (scaled by  $\eta_{3\alpha}$ ) and opacity parameter ( $\zeta_{\text{opacity}}$ ). Increasing  $\eta_{3\alpha}$  does not promote evolution toward the RSG phase and may even suppress it in the low-opacity regime ( $\zeta_{\text{opacity}} \lesssim 10^{-3}$ ).

### 3.3. Grid (d): Shell Hydrogen Burning Rate and Opacity

The reaction rates of H burning can significantly influence whether a star evolves into an RSG; however, it remains unclear whether this effect originates primarily from core H burning during the main-sequence phase or from shell H burning in the post-main-sequence phase. To address this question, we constructed another set of models, Grid (d), in which the CNO cycle reaction rates are modified only during the post-main-sequence shell H-burning phase using  $\eta_{\text{shellCNO}}$ , while remaining unchanged during the main sequence.

Figure 3 shows the resulting  $R_{\max}$  values for models with varying  $\eta_{\text{shellCNO}}$ . Despite some scatter in the data, it is clear that  $\eta_{\text{shellCNO}}$  has little impact on the final radii of supergiants. In general, even when  $\eta_{\text{shellCNO}}$  is extremely low, stars with sufficiently high opacity can still expand to RSG dimensions.

This suggests that the strong dependence of  $R_{\max}$  on  $\eta_{\text{CNO}}$  observed in Grid (c) primarily originates from core H burning during the main sequence, rather than from shell H burning in the post-main-sequence phase. In other words, our results reveal that nuclear burning during the main sequence can significantly affect the degree of envelope expansion during the post-main-sequence stage.

### 3.4. Grid (e): Helium Burning Rate and Opacity

In Ou & Chen (2024), we showed that enhanced He burning can actually suppress the expansion toward the RSG phase. To further demonstrate this effect, we construct a dedicated set of models, Grid (e), in which the triple-alpha reaction rate is scaled by a linear coefficient  $\eta_{3\alpha}$ .

Figure 4 displays the Grid (e) with varying  $\eta_{3\alpha}$  and  $\zeta_{\text{opacity}}$ . In the lower-right region of the diagram, some models with low  $\zeta_{\text{opacity}}$  and high  $\eta_{3\alpha}$  fail to evolve into RSGs. An increased  $\eta_{3\alpha}$  not only fails to promote RSG formation but may even inhibit it, particularly at low opacity.

In summary, we conducted a series of experiments to investigate the effects of opacity and nuclear reaction rates on the formation of RSGs. Our results show that both metallicity-dependent factors, opacity and the H-burning rate during the main-sequence phase, play important roles in promoting the evolution into an RSG, whereas enhanced core He-burning tends to suppress it.

## 4. DIRECT INDICATOR FOR RSG FORMATION

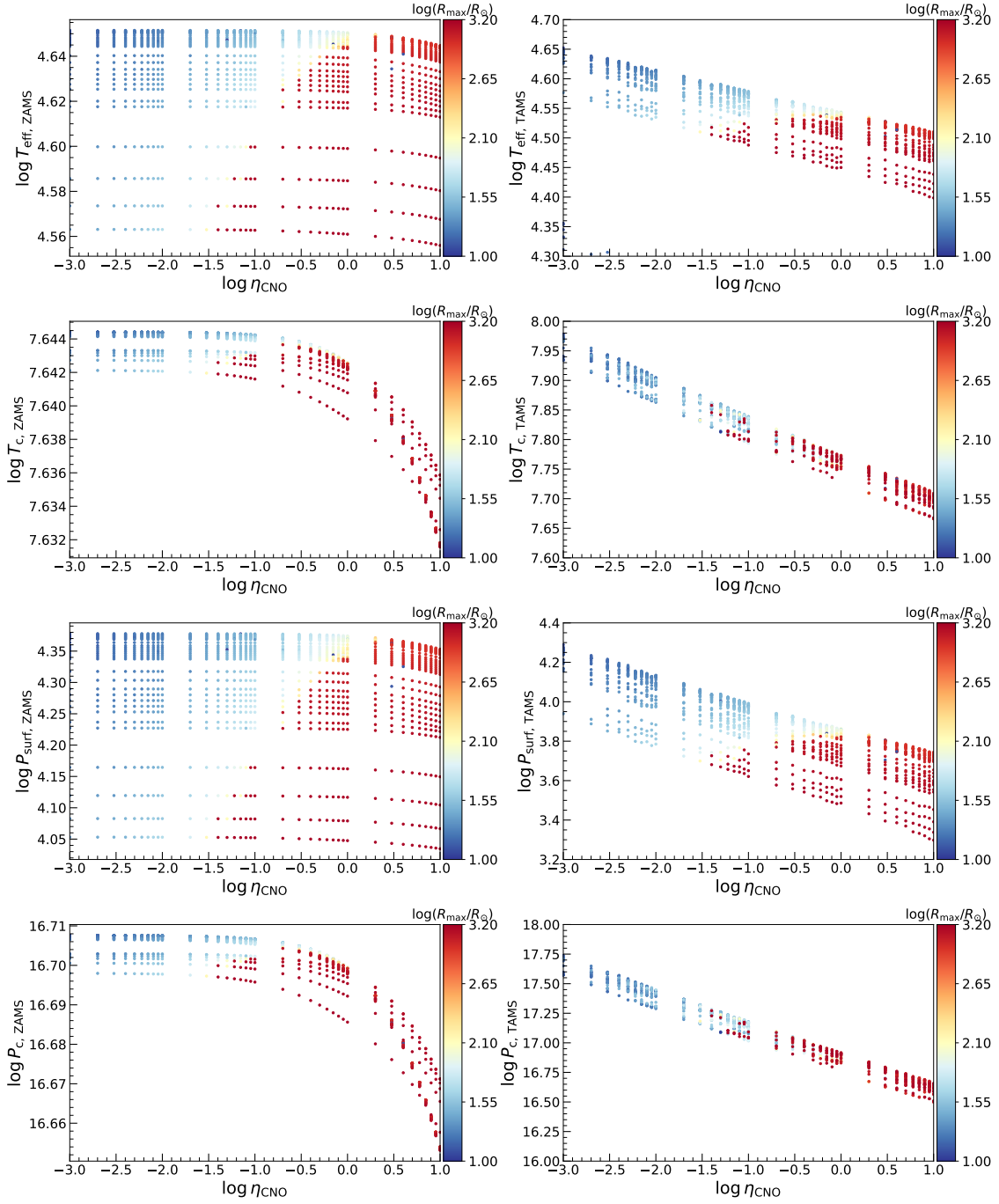


**Figure 5.** Effective temperature ( $T_{\text{eff}}$ ), central temperature ( $T_c$ ), surface pressure ( $P_{\text{surf}}$ ), and central pressure ( $P_c$ ) at both the ZAMS and TAMS for  $25M_{\odot}$  models with  $Z = 0.001$  from Grid (c), where the CNO cycle energy generation rate is scaled by  $\eta_{\text{CNO}}$  and the opacity parameter by  $\zeta_{\text{opacity}}$ . In each panel, models are plotted as functions of  $\eta_{\text{CNO}}$ , and the color of each point represents the maximum stellar radius ( $R_{\text{max}}$ ) reached during the core He-burning phase, with red indicating RSG-scale radii and blue indicating BSG-scale radii.

The results in Section 3 indicate that both opacity and core H-burning rates contribute to promoting stellar evolution into the RSG phase. In this section, we aim to develop a unified picture that explains how these two factors jointly determine whether a star evolves into a red supergiant.

#### 4.1. Threshold for Evolution into the RSG Phase at a Constant Mass

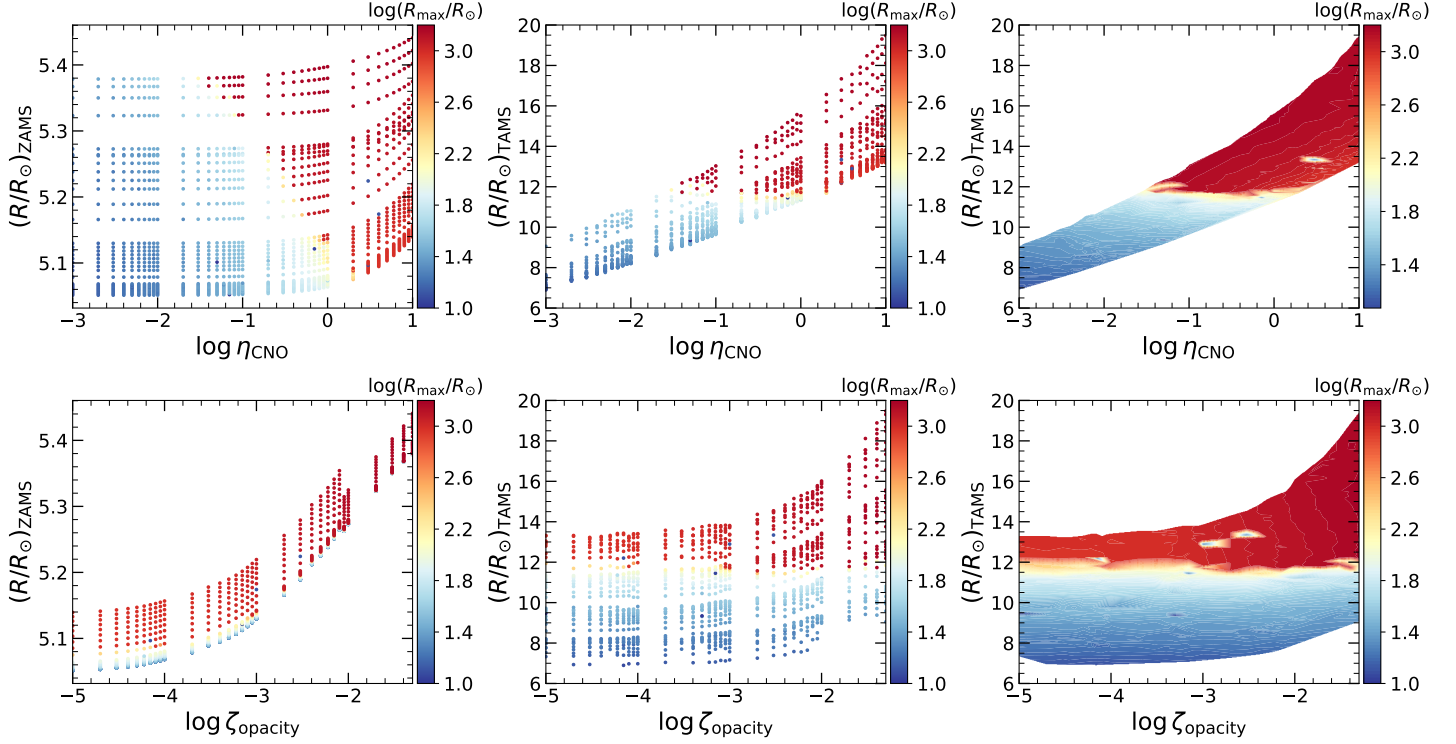


**Figure 6.** ZAMS radii (*left panels*) and TAMS radii (*middle and right panels*) for  $25 M_{\odot}$  models with  $Z = 0.001$  from Grid (c), systematically varying the CNO cycle energy generation rate (scaled by  $\eta_{\text{CNO}}$ ) and the opacity parameter ( $\zeta_{\text{opacity}}$ ). The top row shows models arranged along  $\eta_{\text{CNO}}$ , and the bottom row along  $\zeta_{\text{opacity}}$ . In each panel, colors indicate the maximum radius reached during the core He-burning phase ( $R_{\text{max}}$ ), with red corresponding to RSG sizes and blue to BSG sizes. The middle panels display individual models as scattered points at TAMS, while the right panels present smoothed contour plots using the same dataset. Notably, models with TAMS radii  $\gtrsim 12 R_{\odot}$  predominantly evolve into RSGs, whereas those below this threshold remain BSGs.

One key finding from the previous section is that the H-burning rate during the main-sequence phase significantly influences the star’s post-main-sequence evolution. To investigate this delayed effect of main-sequence processes on post-main-sequence evolution, we analyze how the stellar parameters in the main sequence correlate with the maximum radius ( $R_{\text{max}}$ ) reached during the core He-burning stage. In particular, we examine two key moments in the history of stellar evolution: the ZAMS and the terminal-age main sequence (TAMS).

To avoid the complication of varying stellar mass, we begin with Grid (c), in which the initial mass is fixed at  $25 M_{\odot}$ . Figure 5 shows the effective temperature ( $T_{\text{eff}}$ ), central temperature ( $T_{\text{c}}$ ), surface pressure ( $P_{\text{surf}}$ ), and central pressure ( $P_{\text{c}}$ ) at both the ZAMS and TAMS for each model. The data points are plotted as functions of  $\eta_{\text{CNO}}$ , and colored by the resulting  $R_{\text{max}}$ . Our main goal is to identify the boundary separating models that evolve into RSGs (red points) from those that remain as BSGs (blue points), and to explore how this transition correlates with the physical parameters at ZAMS and TAMS. If a threshold value in one of these parameters can clearly distinguish the red and blue points, it may provide an important clue to the underlying evolutionary mechanism.

At ZAMS, while RSG and BSG models show a clear visual separation, the dividing line does not align with any fixed value of  $T_{\text{eff}}$ ,  $T_{\text{c}}$ ,  $P_{\text{surf}}$ , or  $P_{\text{c}}$ . Thus, these ZAMS parameters alone do not serve as direct predictors of whether a star will become an RSG.

At the TAMS, neither  $T_{\text{c}}$  nor  $P_{\text{c}}$  shows a clear separation between the RSG and BSG models, implying that physical conditions of the stellar core at this stage are also not robust indicators of the final supergiant outcome. Among the physical parameters examined, the most reliable discriminator is the effective temperature at the TAMS. Models with  $T_{\text{eff}} \lesssim 30,000\text{--}35,000\text{K}$  at the TAMS tend to evolve into RSGs, whereas hotter models do not. This suggests that  $T_{\text{eff}}$  at the TAMS serves as a practical threshold for evolution toward the RSG phase.

$T_{\text{eff}}$  is tightly related to the stellar radius as the envelope cools during expansion. Thus, we further examine how the radii at the ZAMS and TAMS correlate with the maximum radius,  $R_{\text{max}}$ . In Figure 6, we present the ZAMS and TAMS radii as functions of  $\eta_{\text{CNO}}$  and  $\zeta_{\text{opacity}}$ , with colors of data points indicating the corresponding values of  $R_{\text{max}}$ .

At the ZAMS, when core H burning has just begun, the stellar radius ( $R_{\text{ZAMS}}$ ) shows minimal dependence on  $\eta_{\text{CNO}}$ , but displays moderate variation with  $\zeta_{\text{opacity}}$ . At this stage, the boundary separating RSG and BSG data points appears as a tilted line rather than aligning with any constant radius. This suggests that the ZAMS radius alone is not a robust predictor of whether a star will eventually evolve into an RSG.

As shown in the middle and right panels of Figure 6, by the TAMS, after the main-sequence evolution is complete, the stellar radius ( $R_{\text{TAMS}}$ ) exhibits a much stronger dependence on  $\eta_{\text{CNO}}$ , while opacity also contributes to increasing the radius to some extent, particularly for  $\zeta_{\text{opacity}} \gtrsim 10^{-3}$ . RSG and BSG models are now clearly divided by a horizontal boundary. Specifically, if the TAMS radius exceeds a threshold of  $\sim 12 R_{\odot}$ , a  $25 M_{\odot}$  star eventually evolves into an RSG; otherwise, it remains a BSG. *These results indicate that the stellar radius attained by the end of the main-sequence phase is a decisive factor for whether a star will ultimately evolve into an RSG.*

To assess whether this threshold radius correlates with the He core radius, we plot the distribution of TAMS stellar radius versus the He core radius at its formation, with point colors indicating  $R_{\text{max}}$ . We find that, for any given TAMS radius, the models span a broad range of core radii. The boundary separating RSGs (red points) from BSGs (blue points) at  $R_{\text{TAMS}} \sim 12 R_{\odot}$  does not align with a unique He core radius, but spans a broad range of core sizes. This confirms that whether a star evolves into an RSG is not determined by He core radius, but rather by the radius of the entire star at the onset of the post-main-sequence phase.

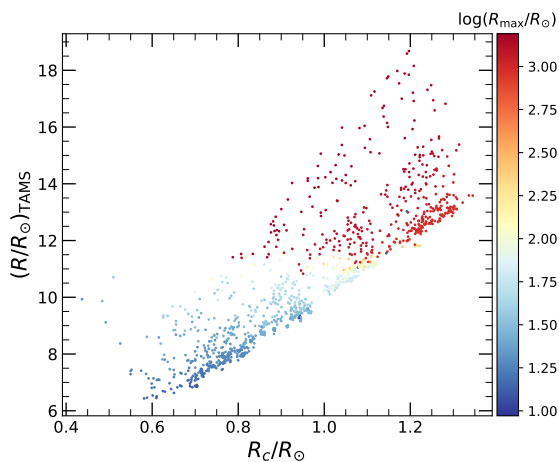


**Figure 7.** Distribution of TAMS radii and He core radii at its formation ( $R_c$ ), with colors indicating the maximum radius during core He burning ( $R_{\text{max}}$ ). The boundary between RSG and BSG models aligns closely with a horizontal line of constant TAMS radius, rather than with the He core radius.

These findings point to a unified principle of the metallicity effect on supergiant evolution. At a fixed initial mass, a star can eventually evolve into an RSG if its radius at the onset of post-main-sequence stage exceeds a certain threshold. Conversely, if the star fails to reach this threshold, it will remain a BSG. Both opacity and the core H-burning rate are influenced by metallicity and affect the stellar structure during the main-sequence phase. Together, they shape the stellar radius at the TAMS, which ultimately determines whether the star will evolve into an RSG.

We note that altering the core He-burning rates during the post-main-sequence phase, as explored in Grid (e), can still influence the final evolutionary outcome. However, it does not account for the systematic trend in which higher metallicity favors RSG formation over BSGs. For this reason, we exclude this effect from our main analysis.

#### 4.2. Threshold TAMS Radii for Different Masses

To investigate how stellar mass influences the threshold radius required for RSG formation, we conduct a similar analysis using Grid (a). We examine the boundary between red and blue data points, which delineates the transition between stars that evolve into RSGs and those that remain BSGs. As shown in the left panel of Figure 8, this boundary is no longer located at a constant TAMS radius but increases systematically with stellar mass.

To obtain a coarse fit for the threshold TAMS radius required for RSG formation as a function of mass, we rescale the TAMS radius ( $R_{\text{TAMS}}$ ) by  $M_{\text{TAMS}}^\alpha$ , where  $M_{\text{TAMS}}$  is the stellar mass at the TAMS and  $\alpha$  is a trial exponent. By manually adjusting  $\alpha$ , we identify a scaling relation that yields an approximately horizontal boundary separating RSG and BSG cases. As shown in the right panel of Figure 8, this leads to the following approximate criterion for RSG formation:

$$\left(\frac{R_{\text{TAMS}}}{R_{\odot}}\right) \gtrsim \left(\frac{M_{\text{TAMS}}}{M_{\odot}}\right)^{3/4}, \quad (1)$$

This relation shows the approximate mass dependence of the threshold radius for RSG formation. Note that  $M_{\text{TAMS}}$  differs only slightly from the initial mass, as mass loss during the main sequence is typically modest.

We propose the TAMS radius as a practical criterion for determining whether a star evolves into the RSG phase. However, the underlying physical mechanism responsible for this threshold, and its connection to metallicity, requires further investigation. In the following sections, we address two key questions:

- (1) How does metallicity affect the stellar radius?
- (2) How does the TAMS radius influence post-main-sequence expansion and define a threshold for RSG formation?

We begin by quantifying how metallicity affect stellar structure and evolution in Section 5, followed by an classification of the evolutionary pathways of supergiants in Section 6. Based on these pathways, we then analyze how the TAMS radius regulates supergiant expansion in Section 7.

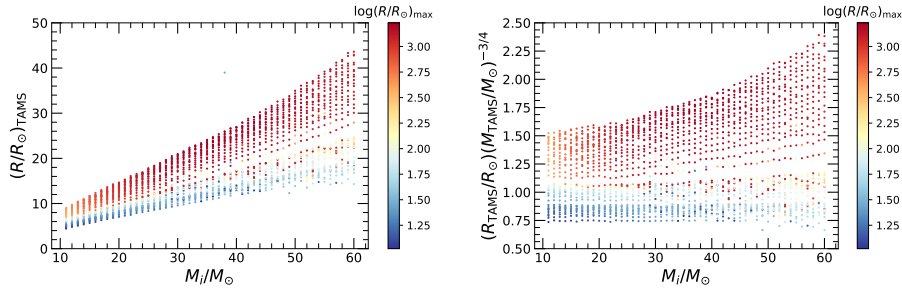


**Figure 8.** The relationship between the TAMS radius and initial stellar mass ( $M_i$ ), with the colors of the data points representing  $R_{\text{max}}$ .

## 5. METALLICITY EFFECT ON STELLAR RADIUS

To evaluate how metallicity affects stellar radius, we begin by analyzing evolutionary tracks from Grids (a) and (c), and then apply homology relations to perform a dimensional analysis.

### 5.1. Metallicity Dependence of Stellar Evolutionary Tracks

In previous sections, we demonstrated that both  $\eta_{\text{CNO}}$  and  $\zeta_{\text{opacity}}$  can influence whether a star evolves into an RSG by modifying its TAMS radius. To investigate how these parameters affect stellar evolution in detail, we examine evolutionary tracks on the HR diagram. We focus on two subsets of models from Grid (c): one in which  $\eta_{\text{CNO}}$  is varied while  $\zeta_{\text{opacity}}$  is held fixed, and the other in which  $\zeta_{\text{opacity}}$  is varied while  $\eta_{\text{CNO}}$  is fixed.

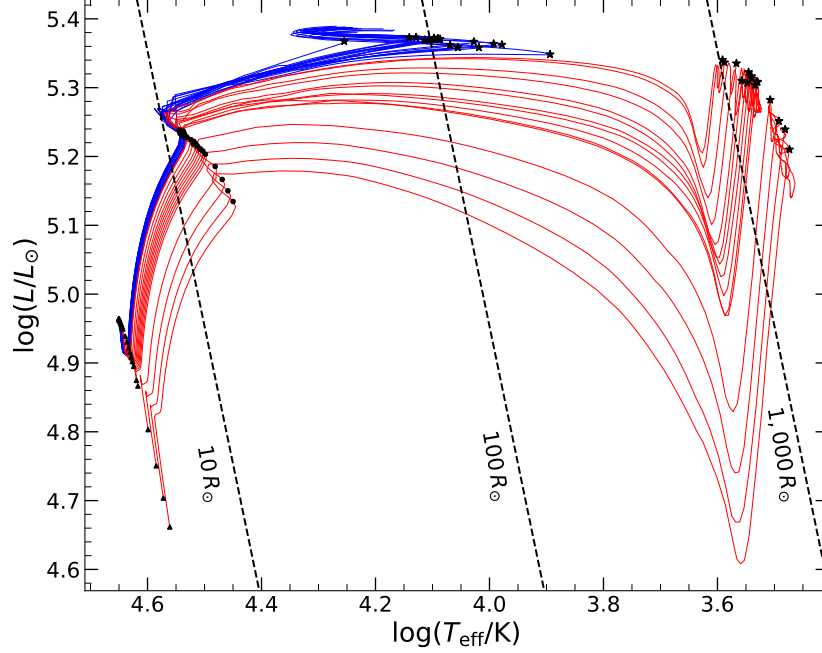
Figure 9 presents the HR diagram for models with an initial mass of  $25 M_{\odot}$  and metallicity  $Z = 0.001$ , where  $\zeta_{\text{opacity}}$  is varied, and the reaction rate of the CNO cycle is fixed at its standard value ( $\eta_{\text{CNO}} = 1$ ). Changes in  $\zeta_{\text{opacity}}$  lead to noticeable differences in luminosity starting from the ZAMS, along with moderate variations in  $T_{\text{eff}}$ . In general, a higher opacity (larger  $\zeta_{\text{opacity}}$ ) results in a lower luminosity, which would suggest a smaller radius. However, higher opacity also reduces  $T_{\text{eff}}$ , partially offsetting the luminosity-driven effect on radius. ZAMS positions lie nearly parallel to iso-radius lines, indicating weak radius sensitivity to opacity at this stage. As the stars evolve, the relationship between opacity and radius shifts. By the time they reach the TAMS, just before the expansion into the supergiant phase, models with higher opacity display systematically larger radii.

Figure 10 displays the HR diagram for another subset of  $25 M_{\odot}$  models at  $Z = 0.001$ , this time with fixed opacity ( $\zeta_{\text{opacity}} = 0.001$ , the standard value for this metallicity) and varying  $\eta_{\text{CNO}}$ . In this case, the ZAMS positions are not significantly affected by changes in  $\eta_{\text{CNO}}$ , but the subsequent evolutionary tracks exhibit a systematic shift in  $T_{\text{eff}}$  across different values of  $\eta_{\text{CNO}}$ . Throughout the main-sequence phase and up to the TAMS, higher values of  $\eta_{\text{CNO}}$  result in lower  $T_{\text{eff}}$ , while the luminosities remain similar. Consequently, stars with enhanced CNO-cycle rates attain larger radii by the TAMS.

These results show that during the main-sequence phase, both increased opacity and a higher CNO-cycle reaction rate shift the stellar evolutionary tracks toward cooler effective temperatures and larger radii on the HR diagram. At higher metallicities, where both the opacity and the CNO-cycle rate are elevated, stars are thus expected to develop systematically larger TAMS radii.

To examine the cumulative effect of metallicity on TAMS radius, Figure 11 presents evolutionary tracks of  $25 M_{\odot}$  models with varying metallicities from Grid (a). While the ZAMS positions show a relatively irregular distribution across different  $Z$ , the

subsequent evolutionary tracks exhibit a more systematic trend toward the TAMS. In general, higher-metallicity models tend to reach lower luminosities but also lower  $T_{\text{eff}}$  at the TAMS, resulting in systematically larger stellar radii. This trend reflects the combined influence of metallicity on stellar evolution through its effects on both opacity and nuclear burning.



**Figure 9.** Evolutionary tracks of  $25 M_{\odot}$ ,  $Z=0.001$  stars with different  $\zeta_{\text{opacity}}$  on the HR diagram. Dashed lines indicate constant-radius contours at 10, 100, and  $1000 R_{\odot}$ . Black triangles mark the ZAMS, black circles indicate the TAMS, and black stars denote the maximum stellar radius reached during the core He-burning phase. Tracks that evolve into RSGs are shown in red, while those that remain BSGs are shown in blue.

### 5.2. Homology Relation between Metallicity and Radius

The effects of opacity and nuclear energy generation rates on stellar radius can be understood through homology relations (see, e.g., Maeder 2009; Kippenhahn et al. 2012). The central idea of the homology method is to compare two stars with similar internal structures. At a given relative mass coordinate, defined as  $\xi = m/M$ , where  $M$  is the total stellar mass and  $m$  is the local mass coordinate, the fundamental physical quantities in the two stars can be transformed with simple scaling constants. In the analysis below, we simply use the global stellar parameters such as  $M$  or the average values within the entire star to express the homology relations to avoid complexity.

The four differential equations governing the stellar structure can be transformed into four homology relations. The mass conservation equation yields

$$M \sim \rho R^3, \quad (2)$$

where  $M$  is the total stellar mass,  $\rho$  is the mean density, and  $R$  is the stellar radius. The hydrostatic equilibrium equation gives

$$P \sim M^2 R^{-4}, \quad (3)$$

where  $P$  is the central pressure. The energy conservation leads to

$$L \sim \epsilon M, \quad (4)$$

where  $L$  is the luminosity and  $\epsilon$  is the average energy generation rate per unit mass. The radiative energy transport equation is:

$$\frac{dT}{dm} = -\frac{3}{64\pi^2 ac} \frac{\kappa l}{r^4 T^3}, \quad (5)$$

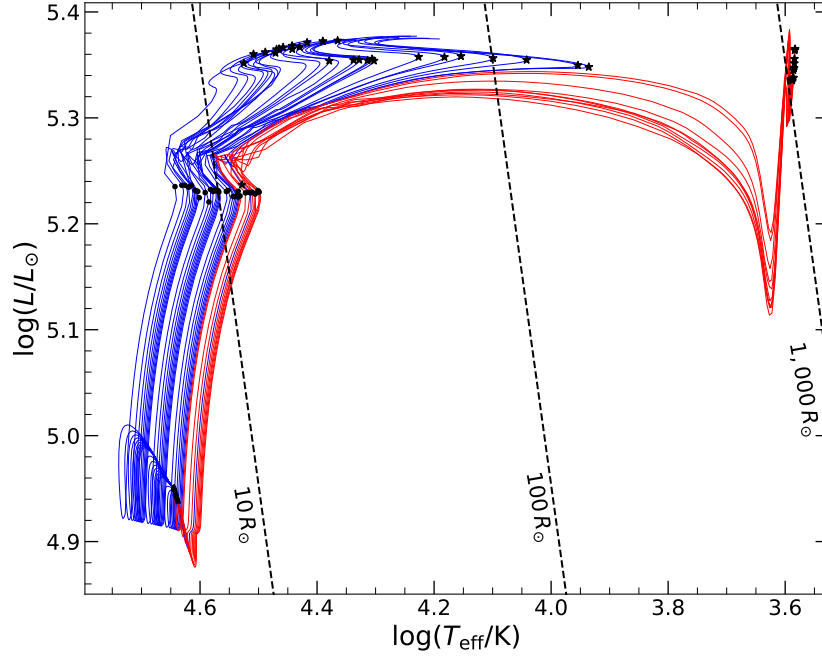


**Figure 10.** Evolutionary tracks of  $25 M_{\odot}$ ,  $Z = 0.001$  stars with different  $\eta_{\text{CNO}}$  on the HR diagram. Dashed lines indicate constant-radius contours at 10, 100, and  $1000 R_{\odot}$ . Black triangles mark the ZAMS, black circles indicate the TAMS, and black stars denote the maximum stellar radius reached during the core He-burning phase. Tracks that evolve into RSGs are shown in red, while those that remain BSGs are shown in blue.

where  $T$  is the temperature,  $\kappa$  is the opacity,  $l$  is the local luminosity,  $a$  is the radiation density constant, and  $c$  is the speed of light. This equation results in the fourth homology relation

$$R \sim (\kappa LM)^{1/4} T^{-1}. \quad (6)$$

Combining Equations (4) and (6), the two relations associated with energy, we obtain

$$RT \sim (\kappa \epsilon)^{1/4} M^{1/2}. \quad (7)$$

Thus, at fixed stellar mass, increasing either  $\epsilon$  or  $\kappa$  leads to a larger product  $RT$ . Since both  $\epsilon$  and  $\kappa$  depend on the metallicity  $Z$ , variations in  $Z$  can significantly affect the stellar structure.

To derive an explicit expression of  $R$  as a function of  $Z$ , we adopt additional assumptions for the gas properties in a star. Following Maeder (2009), we assume:

- An ideal gas equation of state:  $\rho = \frac{\mu m_{\text{H}}}{k} P T^{-1}$ , where  $\mu$  is the mean molecular weight,  $m_{\text{H}}$  is the mass of a H atom, and  $k$  is the Boltzmann constant.
- Kramers' opacity law:  $\kappa = \kappa_0 \rho T^{-3.5}$ , where  $\kappa_0$  is a coefficient that depends on its composition;
- A power-law form for nuclear energy generation rate:  $\epsilon = \epsilon_0 \rho T^{\nu}$ , where  $\epsilon_0$  is a coefficient that depends on its composition, and the exponent  $\nu$  depends on the dominant nuclear reaction. For the CNO cycle,  $\nu = 17$ .

Substituting the expressions for  $\kappa$  and  $\epsilon$  into Equation (7), we obtain:

$$R^{5/2} \sim (\kappa_0 \epsilon_0)^{1/4} T^{\frac{\nu-7.5}{4}} M. \quad (8)$$

To eliminate  $T$ , we use a scaling relation derived by combining mass conservation, hydrostatic equilibrium, and the ideal gas law:

$$T \sim \frac{\mu M}{R}. \quad (9)$$

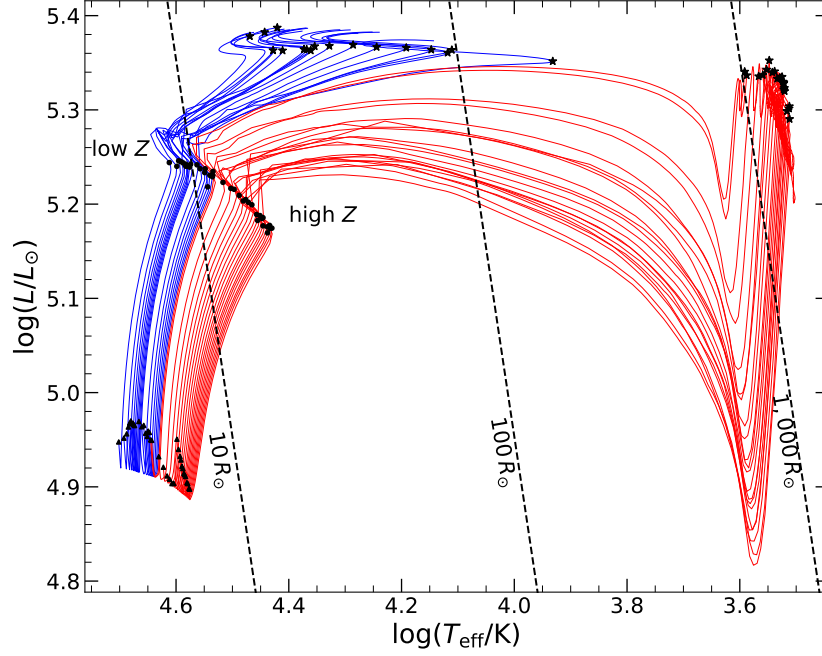


**Figure 11.** Evolutionary tracks of  $25 M_{\odot}$  stars with different metallicities on the HR diagram. Dashed lines indicate constant-radius contours at 10, 100, and  $1000 R_{\odot}$ . Black triangles mark the ZAMS, black circles indicate the TAMS, and black stars denote the maximum stellar radius reached during the core He-burning phase. Tracks that evolve into RSGs are shown in red, while those that remain BSGs are shown in blue.

Substituting this expression for  $T$  into Equation (7) yields:

$$R \sim (\kappa_0 \epsilon_0)^{\frac{2}{2\nu+5}} \mu^{\frac{2\nu-15}{2\nu+5}} M^{\frac{2\nu-7}{2\nu+5}} \quad (10)$$

For  $\nu = 17$  (CNO cycle), this relation becomes:

$$R \sim (\kappa_0 \epsilon_0)^{0.051} \mu^{0.49} M^{0.69}. \quad (11)$$

The three quantities  $\kappa_0$ ,  $\epsilon_0$ , and  $\mu$  all depend on  $Z$ . We now express the  $Z$ -dependence of each term. For Kramers opacity, which includes both free-free and bound-free absorption, the coefficient can be approximated as

$$\kappa_0 \sim (1 + 10^3 Z). \quad (12)$$

When  $Z \gg 10^{-3}$ , bound-free absorption dominates and thus  $\kappa_0 \sim Z$ ; when  $Z \ll 10^{-3}$ , free-free absorption dominates, and thus the opacity becomes largely independent of  $Z$ . Near the critical metallicity  $Z \sim 0.001$  for RSG formation, both contributions are comparable. The coefficient  $\epsilon_0$  for the burning of the CNO cycle is proportional to the mass fraction of carbon, nitrogen, and oxygen, and we approximate it as  $\epsilon_0 \approx Z$ . For a fully ionized ideal gas, the mean molecular weight is approximated by:

$$\mu \simeq \frac{4}{3 + 5X - Z} \quad (13)$$

Assuming a fixed He mass fraction  $Y = 0.278$  in our models, the H mass fraction becomes  $X = 0.722 - Z$ , and thus:

$$\mu^{-1} \simeq \frac{6.61 - 6Z}{4} \quad (14)$$

. Substituting these  $Z$  dependencies into Equation (11), we obtain:

$$R \sim [Z(1 + 10^3 Z)]^{0.051} (1.1 - Z)^{-0.49} M^{0.69}. \quad (15)$$

We define the coefficient dependent on  $Z$  as  $C_Z \equiv [Z(1 + 10^3 Z)]^{0.051} (1.1 - Z)^{-0.49}$ , with contributions from nuclear burning  $C_\epsilon \equiv Z^{0.051}$ , opacity  $C_\kappa \equiv (1 + 10^3 Z)^{0.051}$ , and mean molecular weight  $C_\mu = (1.1 - Z)^{-0.49}$ . The values of these coefficients as functions of  $Z$  are plotted in Figure 12. At  $Z = 2 \times 10^{-2}$ , the value of  $C_Z$  is  $\sim 1.7$  times greater than at  $Z = 10^{-5}$ . Although this difference is somewhat smaller than that seen in the TAMS radii between these two metallicities in Figure 8 ( $\sim 2$ – $3$  times difference between  $Z = 2 \times 10^{-2}$  and  $Z = 10^{-5}$ ), the expression nonetheless captures the general trend of increasing the radius with metallicity.

Among the three components, the contribution from mean molecular weight is relatively mild, as  $(1.1 - Z)^{-0.49}$  remains close to unity and varies only slightly across the metallicity range considered. For  $Z \lesssim 10^{-3}$ , the  $C_\kappa$  also stays near unity, making  $C_\epsilon$  the dominant contributor to  $C_Z$ . At higher metallicities ( $Z \gtrsim 10^{-3}$ ), the contribution from opacity becomes more significant, while  $C_\epsilon$  continues to play a role. This trend is consistent with the results from Grid (b) in Figure 1 and Grid (c) in Figure 2, which show that stellar radii become sensitive to opacity only when  $\zeta_{\text{opacity}} \gtrsim 10^{-3}$ . Here,  $\zeta_{\text{opacity}}$  serves as a pseudo-metallicity parameter used for interpolating opacities in the opacity tables, effectively mimicking the metallicity dependence of opacity. Overall, the increase in stellar radius with metallicity during the main sequence is primarily due to enhanced opacity and more efficient energy generation through the CNO cycle.

We now examine the mass dependence of the stellar radius at fixed metallicity. From the homology relation, we obtain  $R \sim M^{0.69}$  for the CNO cycle. This exponent can be compared to the threshold radius for RSG formation across different stellar masses, as shown in Figure 8, which follows a rough power-law scaling of  $R \sim M^{0.75}$ . Although this exponent 0.75 is only a coarse fit, it matches closely to the exponent 0.69 of the constant-metallicity relation. This similarity indicates that the mass dependence of the threshold radius for RSG formation is closely aligned with mass dependence of stellar radius at constant metallicity. Consequently, the existence of a nearly constant critical metallicity at  $Z \sim 0.001$  across a range of masses can be well justified.

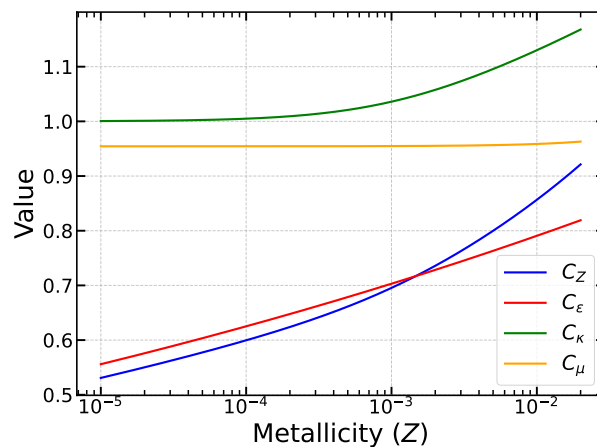


**Figure 12.** The coefficient of radius  $C_Z$  as a function of metallicity, along with the individual contributions from nuclear energy generation ( $C_\epsilon$ ), opacity ( $C_\kappa$ ), and mean molecular weight ( $C_\mu$ ), as derived from homology relations.

## 6. CLASSIFICATION OF SUPERGIANT EVOLUTION PATHWAYS

To understand the origin of the threshold TAMS radius that determines RSG formation, we build on the evolutionary pathways proposed in our previous work [Ou & Chen \(2024\)](#). In that study, we identified two pathways through which stars evolve into the RG/RSG phase, both governed by a refined form of the “mirror principle,” wherein the stellar envelope expands or contracts in the opposite direction of the shell-envelope boundary. Initially, as the shell-envelope boundary recedes inward during core contraction, the envelope expands accordingly. In some models, the envelope expands into the RG/RSG regime during this phase—this represents the first evolutionary pathway to RG/RSG formation.

After core contraction ends, the nuclear energy generation rate ( $L_{\text{nuc}}$ ), which includes contributions from shell H burning and core He burning, dominates the energy production of the stellar interior. Although  $L_{\text{nuc}}$  dominates the energy source during this phase, it is already in decline. As  $L_{\text{nuc}}$  decreases, the shell-envelope boundary continues to move inward, causing the envelope to expand further. If  $L_{\text{nuc}}$  subsequently increases after reaching a minimum, the envelope reverses and contracts, and the star remains a BSG. If, on the other hand,  $L_{\text{nuc}}$  continues to decline monotonically, the envelope continues to expand into the RSG regime, this represents the second pathway to the evolution of RG / RSG.

Based on these evolutionary pathways, we classify each massive star model in Grid (a). In addition to the above scenarios, we identify an additional evolutionary type that occurs in stars with initial masses  $\gtrsim 30M_{\odot}$  and metallicities  $Z \lesssim 0.001$ . In these cases, the C core begins to form while the He core is still contracting. The envelope may or may not expand further after the onset of core C burning, and this complex evolution in the final stages lies beyond the scope of this study. As our classification focuses on the core He-burning stage, we categorize these stars as BSGs on the basis of their status before the formation of the C core.

Combining all cases, we classify the core He-burning evolution of massive stars into four distinct types:

- (1) **RSG-C**: Core contraction directly leads to expansion into the RSG regime.
- (2) **RSG-L**: The luminosity of nuclear burning ( $L_{\text{nuc}}$ ) undergoes a sustained decline after the core contraction, driving a continued expansion of the envelope in the RSG regime.
- (3) **BSG-L**: The luminosity of nuclear burning ( $L_{\text{nuc}}$ ) increases shortly after core contraction, causing the envelope to contract, and the star remains a BSG.
- (4) **BSG-E**: Early C core formation occurs during ongoing He core contraction; the star remains in the BSG phase at this time.

To perform the classification, we examine the evolutionary tracks of each model using the approach described in Section 4 of [Ou & Chen \(2024\)](#). We track the evolution of the stellar radius ( $R_*$ ), central pressure ( $P_c$ ), and the nuclear energy generation rate ( $L_{\text{nuc}}$ ) from the formation of the He core to the formation of the C core. Within this time interval, we identify the maximum stellar radius ( $R_{\text{max}}$ ) and the maximum central pressure ( $P_{\text{max}}$ ), along with the corresponding stellar radius at the time of  $P_{\text{max}}$ , denoted  $R_{P_{\text{max}}}$ .

If  $R_{P_{\text{max}}}$  and  $R_{\text{max}}$  differ by less than 1%, this indicates that the maximum radius is reached while the central pressure is still increasing, indicating that the core is contracting at that time. For stars that satisfy this condition and have an effective temperature  $\log(T_{\text{eff}}/\text{K}) < 3.8$  at  $R_{\text{max}}$ , we classify them as **RSG-C**.

If  $R_{P_{\text{max}}}$  occurs significantly earlier than  $R_{\text{max}}$ , it indicates that the envelope continues to expand after the core contraction ends. In such cases, we identify the minimum  $L_{\text{nuc}}$  following  $R_{P_{\text{max}}}$  and define the corresponding stellar radius at this time as  $R_{L_{\text{min}}}$ . If  $R_{L_{\text{min}}}$  and  $R_{\text{max}}$  differ by less than 5%, we classify the model as **RSG-L** if  $\log(T_{\text{eff}}/\text{K}) < 3.8$  at  $R_{\text{max}}$ , and as **BSG-L** if  $\log(T_{\text{eff}}/\text{K}) \geq 3.8$  at  $R_{\text{max}}$ .

For low-metallicity models, we identify 60 cases where the star remains a BSG throughout core He burning and exhibits  $R_{P_{\text{max}}} \sim R_{\text{max}}$ . These cases cannot be reliably classified using automated criteria. We therefore assign classifications manually based on the evolution of  $R_*$  and  $L_{\text{nuc}}$ . Models that exhibit envelope contraction when  $L_{\text{nuc}}$  reaches the minimum and subsequently rises are classified as **BSG-L**, while those that continue expanding at the time of C core formation are classified as **BSG-E**.

Figure 13 illustrates the classification of each model in Grid (a), along with the corresponding  $R_{\text{max}}$  values. For high-metallicity stars with  $Z \gtrsim 0.01$ , nearly all stars with initial masses  $\geq 25M_{\odot}$  directly expand into the RSG regime during core contraction, via the **RSG-C** pathway. For metallicities in the range  $Z \sim 0.001 - 0.01$ , near the critical metallicity ( $Z_c \sim 0.001$ ), as well as for stars with  $< 25M_{\odot}$  and higher metallicity, many models evolve into RSGs via the **RSG-L** pathway, while others still follow the **RSG-C** pathway. At low metallicities ( $Z \lesssim Z_c \sim 0.001$ ), stars generally remain as BSGs but separate into two categories: stars with  $< 30M_{\odot}$  are mostly **BSG-L**, while those with  $M \gtrsim 30M_{\odot}$  tend to be **BSG-E**.

The critical metallicity for cool supergiant formation presents at  $Z \sim 0.001$  across the full mass range of  $11-60M_{\odot}$ . However, the boundary between the RSG and BSG regimes does not correspond to a single transition between two evolutionary subtypes; rather, it is composed of multiple subtype boundaries that vary with stellar mass. For stars with initial masses below  $30M_{\odot}$ , the critical metallicity corresponds to the transition between the **RSG-L** and **BSG-L** cases, which is well defined at  $Z \sim 0.001$ . The physical mechanisms governing this bifurcation have been thoroughly studied in [Ou & Chen \(2024\)](#). This mass range ( $11-30M_{\odot}$ ) matches the classical red supergiant mass range ([Meynet & Maeder 2000](#); [Beasor et al. 2025](#)), many of which are expected to end their lives as core-collapse supernovae ([Smartt et al. 2009](#)).

In contrast, for stars with  $M \gtrsim 30M_{\odot}$ , the critical metallicity corresponds to the transition between **RSG-C** and **BSG-E** cases. This boundary is less sharply defined, and the evolutionary behavior in this mass regime becomes more complex. We return to discuss the nature of these **BSG-E** models at the end of Section 7.

## 7. ENVELOPE EXPANSION AND CORE CONDITION

To investigate the physical origin of the threshold radius for RSG formation, we examine a set of models with varying values of  $\eta_{\text{CNO}}$  and  $\zeta_{\text{opacity}}$ , focusing on the evolution of their core properties. Figure 14 presents the time evolution of central pressure

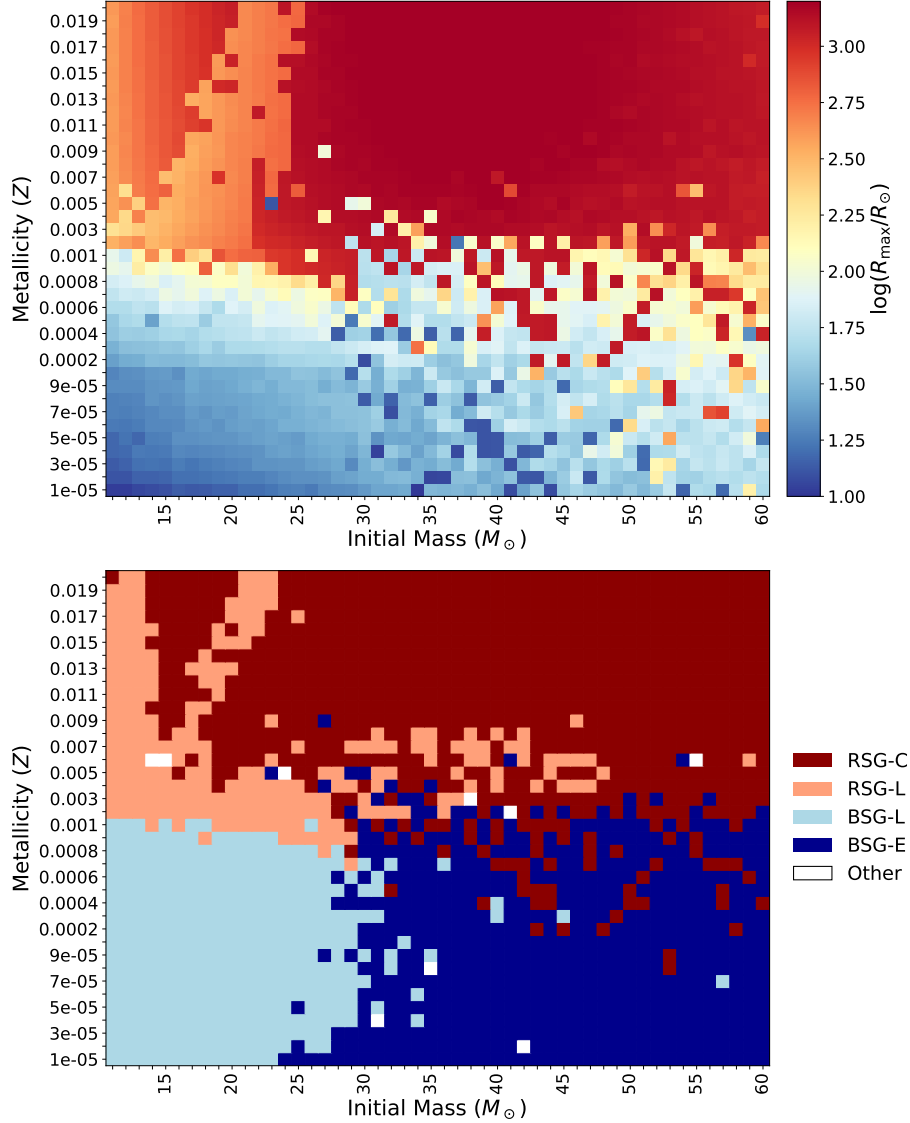


**Figure 13.** *Top panel:* Maximum stellar radius during the core He-burning stage ( $R_{\max}$ ) for each model in Grid (a), spanning initial masses of  $11\text{--}60M_{\odot}$  and metallicities of  $Z = 10^{-5}\text{--}2 \times 10^{-2}$ . *Bottom panel:* Classification of each model’s evolutionary pathway into these types: **RSG-C**, **RSG-L**, **BSG-L**, **BSG-E**, and **Other**. In general, stars with initial masses  $\lesssim 30M_{\odot}$  and metallicities  $Z \lesssim Z_c \sim 0.001$  follow the **BSG-L** pathway, while more massive stars ( $\gtrsim 30M_{\odot}$ ) with at similarly low metallicities are classified as **BSG-E**. Stars with  $Z \gtrsim Z_c$  are classified as either **RSG-C** or **RSG-L**.

( $P_c$ ) along with the stellar radius ( $R_*$ ), illustrating the relationship between the evolution of the core and the expansion of the envelope. The models are sorted by  $R_{\text{TAMS}}$  in the legend, rather than by the individual parameter values of  $\eta_{\text{CNO}}$  or  $\zeta_{\text{opacity}}$ .

All the models in Figure 14 exhibit a common evolutionary trend:  $P_c$  increases significantly and then temporarily stabilizes before continuing to rise. This behavior corresponds to the contraction and stabilization of the He core. During this stages, the envelope expands to BSG or RSG radii, leading to an increase in  $R_*$ . While the overall trend is consistent across models, the tracks are systematically offset in  $R_*$  between models. Importantly, the offset in  $R_*$  across the evolutionary tracks increases systematically with  $R_{\text{TAMS}}$ , rather than with the individual input parameters  $\eta_{\text{CNO}}$  or  $\zeta_{\text{opacity}}$ . In general, models with smaller  $R_{\text{TAMS}}$  reach the end of the core contraction and reach a peak  $P_c$  at smaller stellar radii.

As shown earlier, the TAMS radius is a strong indicator of whether a star will evolve into the RSG phase. We now investigate the physical connection between the TAMS stellar structure and the subsequent evolution into a supergiant. The results in Figure 14 suggest that the core evolution from the TAMS to the supergiant stage may bridge this gap. Stars with smaller TAMS

radii undergo core contraction and stabilization at smaller stellar radii and tend to remain BSGs. In contrast, stars with larger TAMS radii experience core contraction at larger radii and subsequently succeed in expanding to RSG dimensions.

To understand how the shift in envelope size corresponding to a given stage of core evolution influences the fate of supergiants, we refer to the criterion for RSG formation. As discussed in Section 6, for stars with initial masses below  $30M_{\odot}$ , the critical metallicity marks the boundary between the RSG-L and BSG-L regimes. In these cases, whether a star eventually becomes an RSG is primarily governed by the behavior of  $L_{\text{nuc}}$ .

To examine the evolution of  $L_{\text{nuc}}$  in stars with different TAMS radii, Figure 15 presents this evolution for the same set of models shown in Figure 14. These  $25M_{\odot}$  models follow the typical evolutionary paths of the RSG-L and BSG-L regimes. The bifurcation occurs during the BSG phase: if  $L_{\text{nuc}}$  begins to rise while the envelope is still compact, envelope expansion halts, and the star remains a BSG. Conversely, if  $L_{\text{nuc}}$  continues to decline, the envelope expands further, and the star evolves into the RSG phase.

In the same figure, we also plot the individual contributions from the luminosity of H ( $L_{\text{H}}$ ) and the luminosity of the He ( $L_{\text{He}}$ ). Comparing the RSG and BSG models near the peak of  $L_{\text{nuc}}$ , we find no significant differences in the rate of decline of  $L_{\text{H}}$ . However, the evolution of  $L_{\text{He}}$  reveals a marked contrast. In models that remain BSGs,  $L_{\text{He}}$  exhibits a sharp increase during the BSG phase, and this increase is responsible for the subsequent upturn in  $L_{\text{nuc}}$ . This rise in  $L_{\text{nuc}}$  causes the shell-envelope boundary to move outward. This motion, in turn, drives the envelope contraction and prevents the star from expanding into the RSG phase.

In fact, the further increase in  $L_{\text{He}}$  occurs not only in the BSG models but also in the RSG models. In Figure 16, we plot the evolution of  $P_{\text{c}}$  and  $L_{\text{He}}$  as functions of time for representative RSG and BSG models. During the core He-burning phase, both models exhibit similar evolutionary trends. Initially, both  $P_{\text{c}}$  and  $L_{\text{He}}$  rise rapidly due to core contraction. As the core contraction concludes,  $P_{\text{c}}$  temporarily decreases before gradually increasing again, while  $L_{\text{He}}$  continues to rise. After reaching its peak,  $L_{\text{He}}$  steadily declines. These features are common to both models, indicating that the core evolution follows a similar trajectory, regardless of whether the star ultimately becomes a RSG or a BSG.

The crucial distinction between RSG and BSG models lies in the timing of the  $L_{\text{He}}$  rise relative to envelope expansion. In RSG models, the further rise in  $L_{\text{He}}$  occurs after the star has already expanded into the stable RSG phase, and thus has little impact on the envelope structure. In contrast, if this increase occurs while the star is still at smaller radii, it can halt the envelope expansion and cause the star to remain in the BSG phase.

Broadly speaking, the primary difference between the models that leads to the bifurcation into RSG and BSG outcomes lies in the correspondence between the evolutionary stages of the core and the envelope. As summarized in the flow chart in Figure 17, the post-main-sequence evolution of the core and the envelope is not synchronized; each follows its own sequence of structural transitions. For the envelope, it initially enters the BSG phase and may subsequently expand into the RSG regime. For the core, evolution begins with contraction starting from the TAMS, followed by a decrease in  $L_{\text{nuc}}$  once the core contraction ends. Afterward,  $L_{\text{He}}$  continues to rise, which can cause an upturn in  $L_{\text{nuc}}$ . If the envelope is still in the BSG phase at this stage, the increase in  $L_{\text{nuc}}$  can lead to envelope contraction, preventing further expansion into the RSG regime. Thus, the timing of these core changes relative to the expansion state of the envelope ultimately determines whether the star evolves into a BSG or an RSG.

So far, our discussion has primarily focused on the **RSG-L** and **BSG-L** evolutionary types. The **BSG-E** type can also be understood through the correspondence between the evolution of the core and the envelope. In low-metallicity stars with initial masses  $\gtrsim 30M_{\odot}$ , which fall into the BSG-E type, the envelope remains compact, confined within the BSG regime, while the core not only undergoes He burning, but has already advanced to the core C-burning stage. Once a star enters the core C burning, its evolution becomes significantly more complex compared to the earlier stages. As shown in Figure 8 of Paper I, the evolutionary outcomes of low-metallicity models beyond the onset of core C burning become highly irregular. The fundamental reason these stars evolve into the **BSG-E** type is that their small envelope radii correspond to an advanced core evolutionary stage.

As summarized in Figure 17, the four evolutionary pathways originates from different correspondence between core condition and envelope radius. The **RSG-C** pathway is followed by stars with large TAMS radii, such that even modest expansion during core contraction is sufficient for the star to enter the RSG phase. If the TAMS radius is smaller than that of **RSG-C** cases but still exceeds the threshold radius for RSG formation, the star follows the **RSG-L** pathway. In this case, the envelope expands to the BSG regime when core contraction ends and continues expanding toward the RSG phase as the H-burning shell moves inward, driven by the continued decline of  $L_{\text{nuc}}$ . We note that once a star reaches the RSG phase, it stabilizes there and is no longer affected by subsequent changes in the core during advanced He burning.

For stars  $\lesssim 30M_{\odot}$ , if the TAMS radius is below the threshold for RSG formation, the star follows the **BSG-L** pathway. For this type, the envelope expands to the BSG radius when the core enters the advanced He-burning stage with further rise of  $L_{\text{He}}$ , and thus the upturn of  $L_{\text{nuc}}$ . The increase of  $L_{\text{nuc}}$  shifts the H-burning shell outward and causes the envelope to contract, resulting

in the star remaining as a BSG. Finally, the **BSG-E** pathway applies to more massive stars ( $\gtrsim 30M_{\odot}$ ) with TAMS radii below the threshold of RSG formation. They remain compact and enter core C burning while the He core is still contracting.

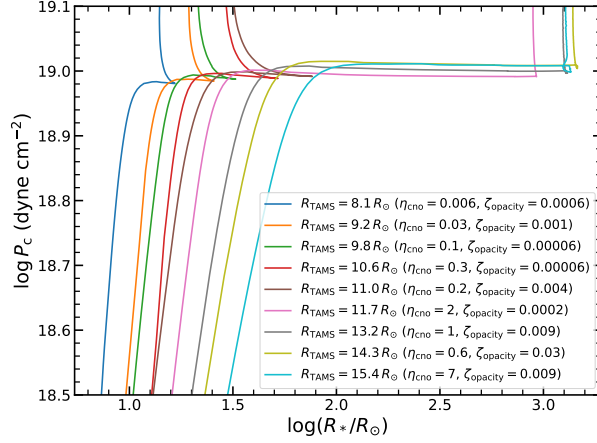


**Figure 14.** Evolution of central pressure ( $P_c$ ) as a function of stellar radius ( $R_*$ ) during the core He-burning stage for  $25M_{\odot}$ ,  $Z = 0.001$  models with varying  $\eta_{\text{CNO}}$  and  $\zeta_{\text{opacity}}$ . The legend is ordered by the TAMS radius ( $R_{\text{TAMS}}$ ) of each model. Notably, the horizontal shifts in  $R_*$  among the evolutionary tracks align with  $R_{\text{TAMS}}$ , rather than with the individual input parameters  $\eta_{\text{CNO}}$  or  $\zeta_{\text{opacity}}$ .

## 8. DISCUSSIONS AND CONCLUSIONS

Stellar models indicate a critical metallicity of  $Z_c \sim 0.001$  that determines whether a star successfully evolves into the RSG phase. In this study, we provided a comprehensive physical explanation for the origin of this critical metallicity. Through experiments with  $25M_{\odot}$  models in which we vary opacity and nuclear reaction rates, we identify a threshold TAMS radius that predicts whether a star will expand into the RSG regime. Furthermore, we demonstrate that the mass dependence of this threshold radius is similar to the mass dependence of stellar radius at fixed metallicity, which naturally explains why the critical metallicity for RSG formation remains approximately constant at  $Z \sim 0.001$  across a wide range of stellar masses.

Metallicity significantly influences stellar evolution through its effects on opacity, nuclear reaction rates, and the mean molecular weight. Based on evolutionary tracks from stellar models, along with dimensional analysis using homology relations, we have shown that stars with higher metallicities tend to develop larger radii upon entering the post-main-sequence stage. This behavior is primarily driven by enhanced opacity and increased CNO-cycle energy generation at higher  $Z$ . As metallicity affects the TAMS radius, and the TAMS radius sets a threshold for RSG formation, metallicity ultimately determines whether a star expands into the RSG regime during post-main-sequence evolution.

We further identify the physical mechanism linking the TAMS radius to supergiant outcomes. Generally, the envelope radius corresponding to a given core evolution stage is the key that leads to bifurcation in supergiant evolution. For stars with initial masses in the range  $11\text{--}30M_{\odot}$ , the distinction between the RSG and BSG regimes is primarily governed by the post-main-sequence behavior of  $L_{\text{nuc}}$ . In this mass range, the critical metallicity marks the boundary between the **RSG-L** and **BSG-L** types. If  $Z < Z_c$ , the star has a TAMS radius smaller than the threshold, and the envelope remains compact when a rise in  $L_{\text{He}}$  triggers an upturn in  $L_{\text{nuc}}$ . This upturn drives the shell-envelope boundary outward, triggering envelope contraction and preventing expansion into the RSG regime. In contrast, if a star has  $Z > Z_c$ , its TAMS radius is larger than the threshold, so  $L_{\text{nuc}}$  continues to decline after the core contraction ends, allowing the envelope to continue expanding into the RSG regime. In these cases, the subsequent rise in  $L_{\text{He}}$  occurs after the star has already reached the RSG phase, and therefore has little impact on the envelope structure.

For more massive stars ( $\gtrsim 30M_{\odot}$ ), the threshold metallicity for RSG formation is less sharply defined but still lies near  $Z \sim 0.001$ , as set by the boundary between the **RSG-C** and **BSG-E** regimes. In these low-metallicity stars, the envelope remains compact during the BSG phase, while the core evolves beyond core He burning into the core C-burning stage. After this point, stellar evolution becomes highly irregular, and whether the envelope ultimately expands beyond the BSG stage varies significantly across models.

In addition to metallicity, other factors, such as rotation, can also influence stellar evolutionary tracks on the HR diagram starting from the main-sequence stage (e.g., [Maeder 2009](#)). These effects may alter the envelope radius corresponding to a given stage of core evolution. In particular, the TAMS radius can be affected and potentially shifted above or below the threshold

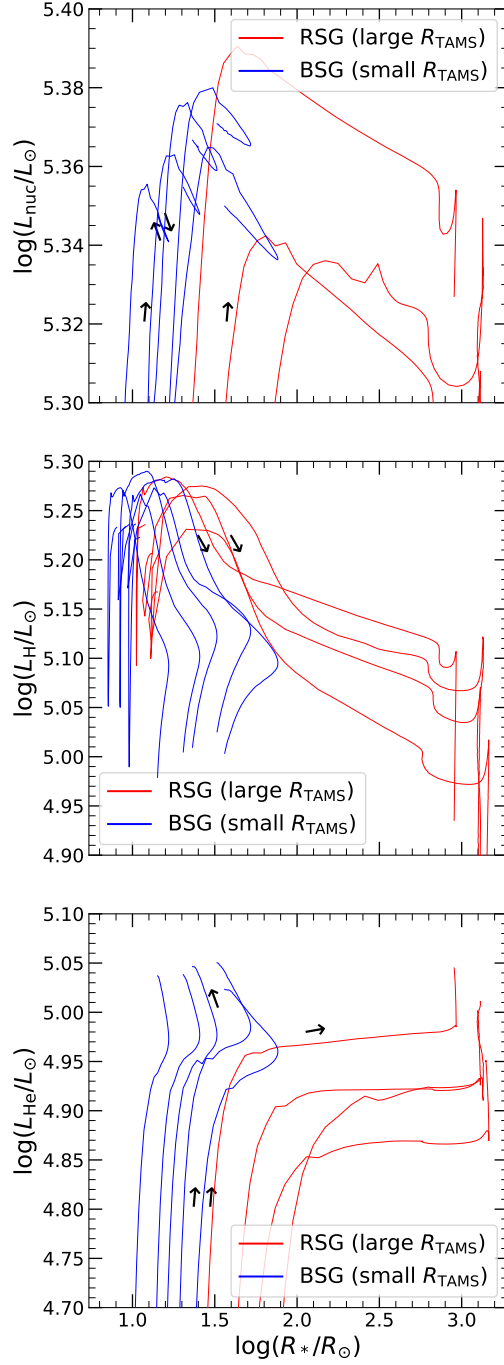


**Figure 15.** Evolution of  $L_{\text{nuc}}$ ,  $L_{\text{H}}$ , and  $L_{\text{He}}$  as functions of stellar radius ( $R_*$ ) for the same models shown in Figure 14. Red curves represent models that evolve into the RSG phase, while blue curves correspond to those that remain in the BSG phase. To avoid clutter, the curves are truncated at the point where  $L_{\text{He}}$  reaches its maximum value.

required for evolution into the RSG phase. In this context, one may expect not only a critical metallicity but also threshold values in other physical parameters, such as rotation velocity, that determine whether a star evolves into an RSG.

From stellar models, we have identified the physical mechanism that causes low-metallicity massive stars to remain blue rather than evolving into the RSG phase. These distinct evolutionary pathways at low metallicity have important implications for the

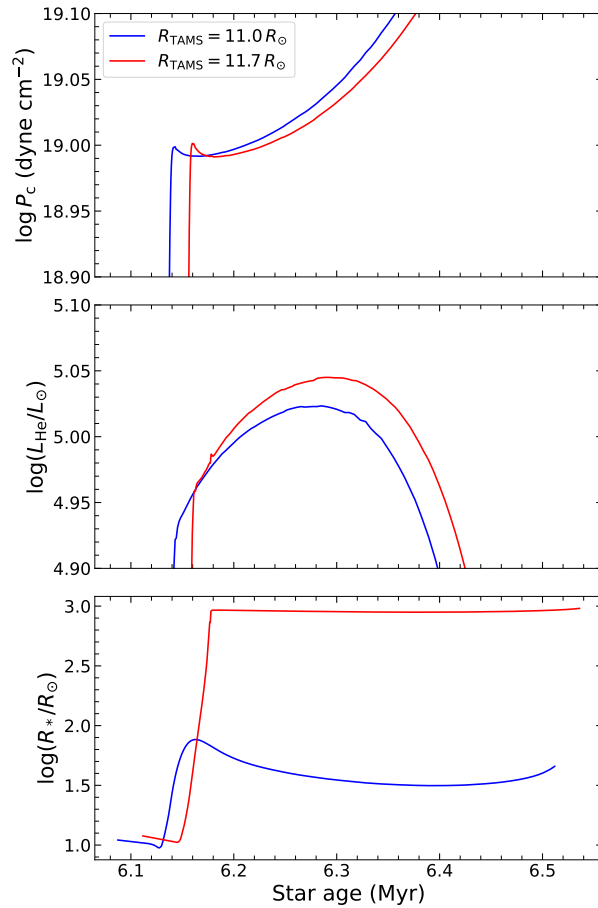


**Figure 16.** Evolution of central pressure ( $P_c$ ), He-burning luminosity ( $L_{\text{He}}$ ), and stellar radius ( $R_*$ ) during the core He-burning stage. The red curves correspond to the model with  $R_{\text{TAMS}} = 11.7 R_{\odot}$ , which evolves into the RSG phase, while the blue curves represent the model with  $R_{\text{TAMS}} = 11.0 R_{\odot}$ , which remains in the BSG phase.

nature of stellar populations and feedback in the early universe. For example, since low-metallicity stars are less likely to evolve into RSGs, a major progenitor class for core-collapse supernovae, the resulting supernova types in metal-poor galaxies may differ significantly from those observed in the local universe. Future observations targeting galaxies with metallicities as low as  $\sim 0.1 Z_{\odot}$  will be crucial in testing these predictions.

This research is supported by the National Science and Technology Council, Taiwan, under grant No. MOST 110-2112-M-001-068-MY3, NSTC 113-2112-M-001-028-, and the Academia Sinica, Taiwan, under a career development award under grant No. AS-CDA-111-M04. This research was supported in part by grant NSF PHY-2309135 to the Kavli Institute for Theoretical Physics (KITP) and grant NSF PHY-2210452 to the Aspen Center for Physics. KC acknowledges the support of the Alexander von Humboldt Foundation. Our computing resources were supported by the National Energy Research Scientific Computing Center (NERSC), a U.S. Department of Energy Office of Science User Facility operated under Contract No. DE-AC02-05CH11231 and the TIARA Cluster at the Academia Sinica Institute of Astronomy and Astrophysics (ASIAA).

*Software:* MESA (Paxton et al. 2011, 2013, 2015, 2018, 2019; Jermyn et al. 2023)

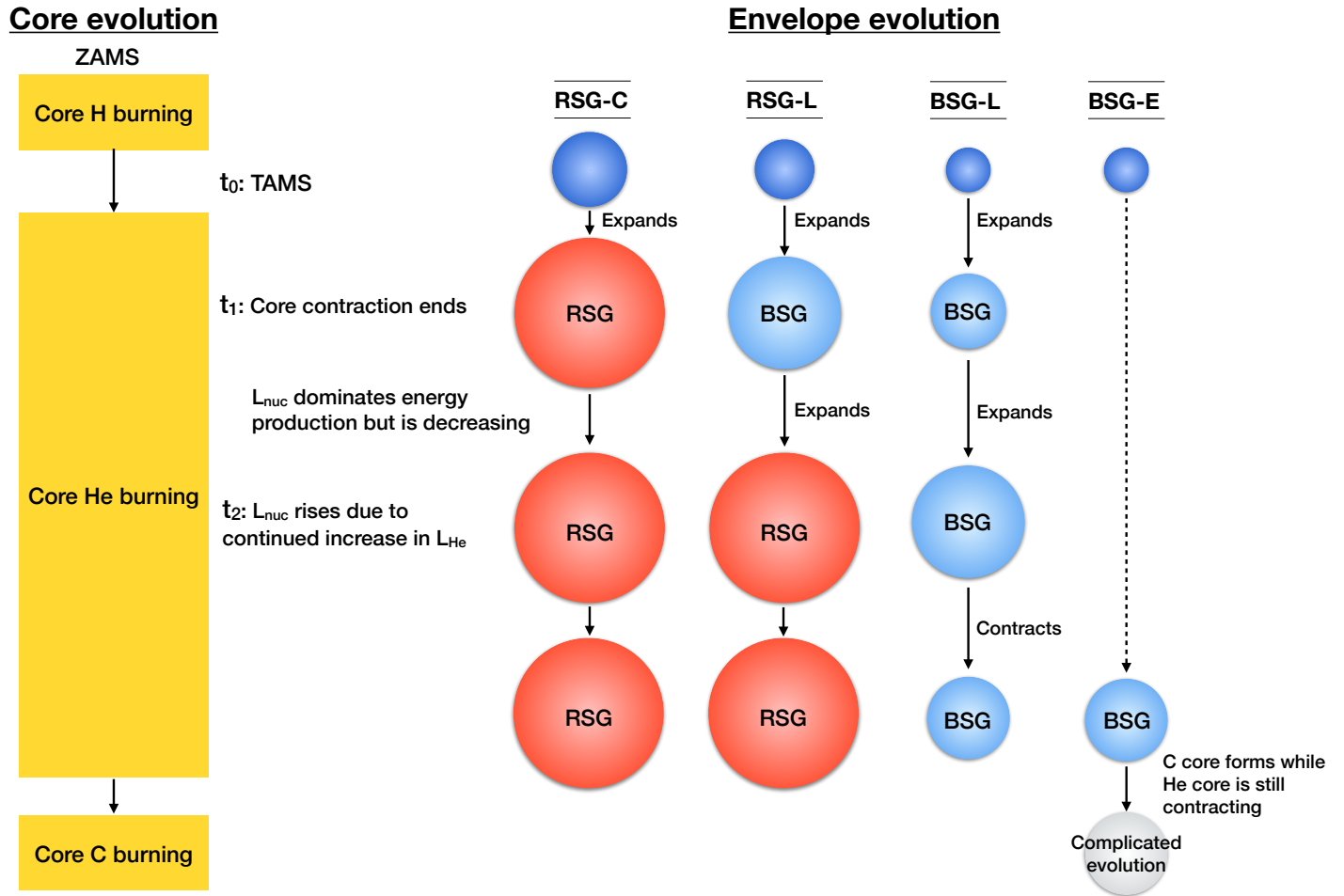


**Figure 17.** Flow chart illustrating the evolutionary stages of the stellar core and envelope. The envelope radius at the TAMS determines the evolutionary pathway and the resulting supergiant type.

## REFERENCES

- Asplund, M., Grevesse, N., Sauval, A. J., et al. 2009, *ARA&A*, The Chemical Composition of the Sun, 47, 1, 481. doi:10.1146/annurev.astro.46.060407.145222
- Arnett, D. 1991, *ApJ*, 383, 295. doi:10.1086/170786
- Baraffe, I. & El Eid, M. F. 1991, *A&A*, 245, 548
- Beasor, E. R., Smith, N., & Jencson, J. E. 2025, *ApJ*, The Red Supergiant Progenitor Luminosity Problem, 979, 2, 117. doi:10.3847/1538-4357/ad8f3f
- Miller Bertolami, M. M. 2022, *ApJ*, A Red Giants' Toy Story, 941, 2, 149. doi:10.3847/1538-4357/ac98c1
- Brocato, E. & Castellani, V. 1993, *ApJ*, 410, 99. doi:10.1086/172729
- Brunish, W. M. & Truran, J. W. 1982, *ApJS*, 49, 447. doi:10.1086/190806
- Eggleton, P. P. & Cannon, R. C. 1991, *ApJ*, 383, 757. doi:10.1086/170833
- El Eid, M. F., The, L.-S., & Meyer, B. S. 2009, *SSRv*, 147, 1. doi:10.1007/s11214-009-9517-6
- Faulkner, J. 2005, *The Scientific Legacy of Fred Hoyle*, 149
- Groh, J. H., Ekström, S., Georgy, C., et al. 2019, *A&A*, 627, A24
- Hirschi, R. 2007, *A&A*, 461, 571
- Iben, I. 1993, *ApJ*, 415, 767. doi:10.1086/173200
- Jermyn, A. S., Bauer, E. B., Schwab, J., et al. 2023, *ApJS*, 265, 15. doi:10.3847/1538-4365/acae8d
- Kippenhahn, R., Weigert, A., & Weiss, A. 2012, *Stellar Structure and Evolution*. ISBN: 978-3-642-30304-3. Berlin, Heidelberg: Springer Berlin Heidelberg, 2012.. doi:10.1007/978-3-642-30304-3
- Limongi, M. 2017, *Handbook of Supernovae*, 513
- Maeder, A. 2009, *Physics, Formation and Evolution of Rotating Stars*, Astronomy and Astrophysics Library. ISBN 978-3-540-76948-4. Springer Berlin Heidelberg, 2009. doi:10.1007/978-3-540-76949-1
- Meynet, G. & Maeder, A. 2000, *A&A*, Stellar evolution with rotation. V. Changes in all the outputs of massive star models, 361, 101. doi:10.48550/arXiv.astro-ph/0006404
- Miller Bertolami, M. M. 2022, *ApJ*, 941, 149. doi:10.3847/1538-4357/ac98c1
- Ou, P.-S. & Chen, K.-J. 2024, arXiv:2407.21383. doi:10.48550/arXiv.2407.21383
- Ou, P.-S., Chen, K.-J., Chu, Y.-H., et al. 2023, *ApJ*, 944, 34. doi:10.3847/1538-4357/aca96e
- Paxton, B., Smolec, R., Schwab, J., et al. 2019, *ApJS*, 243, 10
- Paxton, B., Schwab, J., Bauer, E. B., et al. 2018, *ApJS*, 234, 34
- Paxton, B., Marchant, P., Schwab, J., et al. 2015, *ApJS*, 220, 15
- Paxton, B., Cantiello, M., Arras, P., et al. 2013, *ApJS*, 208, 4
- Paxton, B., Bildsten, L., Dotter, A., et al. 2011, *ApJS*, 192, 3
- Renzini, A. 2023, *MNRAS*, 521, 524. doi:10.1093/mnras/stad159
- Renzini, A. & Ritossa, C. 1994, *ApJ*, 433, 293. doi:10.1086/174645
- Renzini, A., Greggio, L., Ritossa, C., et al. 1992, *ApJ*, 400, 280. doi:10.1086/171995
- Renzini, A. 1984, *Observational Tests of the Stellar Evolution Theory, Selected Topics on the Evolution of Low and Intermediate Mass Stars*, 105, 21.
- Ritossa, C. 1996, *MNRAS*, 281, 970. doi:10.1093/mnras/281.3.970
- Smartt, S. J., Eldridge, J. J., Crockett, R. M., et al. 2009, *MNRAS*, The death of massive stars - I. Observational constraints on the progenitors of Type II-P supernovae, 395, 3, 1409. doi:10.1111/j.1365-2966.2009.14506.x
- Sugimoto, D. & Fujimoto, M. Y. 2000, *ApJ*, 538, 837. doi:10.1086/309150